Composite Structure of Plumes in Stratus-topped Boundary Layers

CHIN-HOH MOENG

National Center for Atmospheric Research, Boulder, Colorado*

ULRICH SCHUMANN

DLR, Institute of Atmospheric Physics, Oberpfaffenhofen, Federal Republic of Germany

(Manuscript received 15 October 1990, in final form 25 April 1991)

ABSTRACT

Knowledge of convective plumes within the clear convective boundary layer (CBL) is quite advanced owing to direct measurements, tank experiments, and large-eddy simulation studies. As a result, modeling of the CBL is relatively successful. Progress for the stratus-topped boundary layer (STBL), however, is slow. This study compares the plume structure of the surface-heated CBL with that of the cloud-top–cooled STBL in the hope of extending our knowledge of the CBL to the STBL.

A conditional sampling technique is applied to the STBL flow fields that are generated through large-eddy simulations, so that the structures of typical updrafts and downdrafts may be derived. For the purpose of comparing the surface-heated CBL and the cloud-top–cooled STBL, an idealized STBL is simulated where the turbulence is maintained solely by cloud-top radiative cooling. The principal difference between the CBL and this idealized STBL lies in the origin of the plumes: primary plumes in the CBL are generated at a rigid surface, while those in the STBL are generated at the entraining interface. It was found that in the idealized STBL, the compensating updrafts are nearly as strong as the top-cooling–generated downdrafts, and they contribute a significant amount to the heat, moisture, and momentum transports. This differs very much from the CBL, where the compensating downdrafts are much weaker than the surface-heating–generated updrafts and contribute much less to the transports. The mechanism that results in such an asymmetry between the CBL and STBL is examined, and suggestions on how the asymmetry affects the entrainment process are made.

1. Introduction

Within the buoyancy-driven planetary boundary layer (PBL), energetic eddies are responsible for most of the transport of momentum, heat, and other scalars. These eddies are variously referred to as *thermals, convective elements, plumes, coherent eddies,* etc. In the clear convective boundary layer (CBL), the dominant convective plumes are the heating-generated updrafts, which scale with the CBL depth, z_i, and the convective velocity,

$$w_* \equiv \left(\frac{g}{T_0} z_i \overline{w\theta}_0\right)^{1/3},$$

where g/T_0 is the buoyancy coefficient and $\overline{w\theta}_0$ is the surface buoyancy flux (e.g., Lenschow and Stephens 1980; Greenhut and Khalsa 1987; Young 1988; Schmidt and Schumann 1989). In this case, where turbulence is driven by bottom heating, updrafts rise much quicker and, consequently, cover an area smaller than downdrafts. If the turbulence is driven by the top cooling only, the flow field should be exactly symmetric (in the upside-down sense) to that in the bottom-heated case—if the top boundary is also a rigid surface (e.g., a channel flow); that is, the primary plumes are now the downdrafts with the same properties as the updrafts in the bottom-heated case. In a stratus-topped boundary layer (STBL) with weak shear, turbulence is mainly driven by the longwave radiative cooling at cloud top. For this reason, one expects the STBL and the CBL to behave symmetrically in the above-described sense. However, in reality the boundary layers also contain asymmetric parts: first, the STBL's top-cooled surface (a free, entraining interface) is not analogous to the CBL's bottom-heated surface (a rigid wall); second, the cloud-top radiative cooling is vertically distributed, rather than being confined to a thin layer. In reality, some STBLs are dominated by other processes like latent heating, surface heating, and internal solar radiative heating, which further destroy the symmetry between the CBL and the STBL; we do not consider these types of STBL here.

In this paper, we investigate the following questions: What are the spatial structures and properties of plumes within the STBL? When downdrafts in the STBL are

* The National Center for Atmospheric Research is sponsored by the National Science Foundation.

Corresponding author address: Dr. C-H Moeng, NCAR/MMM, P.O. Box 3000, Boulder, CO 80307-3000.

generated only by cloud-top cooling at the interface, how do they differ from updrafts in the CBL? How do compensating updrafts in the cloud-top–cooled case differ from compensating downdrafts in the CBL? Some studies have shown that in the CBL, updrafts enhance the entrainment process through penetration into the overlying inversion (Deardorff et al. 1969; Stull 1973; Kaimal et al. 1976; Mahrt 1979). What are the relative roles of updrafts and downdrafts in enhancing the entrainment process in the STBL?

Nicholls (1989) examined the structure of convective downdrafts within the STBL by conditionally sampling aircraft data from a marine stratus-topped boundary layer that is driven mainly by the cloud-top radiative cooling. He found that the convective elements in the STBL have a cellular pattern near the cloud top with narrow downdrafts surrounded by broad updrafts, similar to those found near the surface in the CBL (narrow updrafts surrounded by broad downdrafts). This indicates some symmetry between the surface-heated and cloud-top–cooled cases. However, he pointed out that the downdrafts within the STBL cover a fractional area larger than the updrafts in the CBL studied by Lenschow and Stephens (1980) and Greenhut and Khalsa (1987). Nicholls also suggested that the downdrafts in the STBL do not seem to form "simply as a result of the most negatively buoyant regions sinking," but seem to result from the convergence of horizontal flows near the cloud top. These latter observations suggest an asymmetry between the surface-heated and cloud-top–cooled cases.

In this paper, we discuss the structure of the convective plumes in the large-eddy simulation (LES) version of the STBL. Our sampling technique is a three-dimensional (3D) conditional sampling developed by Schmidt and Schumann (1989), described in section 2. We have performed four large-eddy simulations (A, B, C, and D) of the STBL, which have $(80)^3$ equidistant grid points over a 5 km × 5 km × 1 km domain, with a numerical time step of 1 s. The LES code is described in Moeng (1984, 1986). Simulations A and C were started from an initial state with no turbulent flow and were run for at least 4250 simulation seconds, while B and D were started from the 2500-s turbulent flow of simulation C and were run for 1750 additional simulation seconds. The last 1500-s results were recorded at a 250-s interval for analysis. In all simulations, the large-eddy-turnover time is ~500 s.

As a first step toward understanding the STBL, we exclude solar radiation to eliminate the possible complications as detached or double cloud layers. The longwave radiation parameterization used in this study was described by Moeng and Arakawa (1980) and Moeng (1986): it uses Rodgers' (1967) empirical formula for the water vapor emissivity and the graybody absorber assumption for the cloud-drop emissivity. The radiation calculation requires a large amount of computation time; it uses about half of the computation time in this LES code. For that reason, we stay with the simplest emissivity approach.

Simulation A includes all the processes that are likely to be important in the nocturnal STBL: surface fluxes, longwave radiative cooling, and latent heating; its statistics were reported by Schumann and Moeng (1991a) and compared to experimental results. In section 3, the mean and transport properties of the composite updraft and downdraft of simulation A are examined. Simulation B excludes the latent-heat effect. This "dry cloud" (or "dust cloud") simulation code differs from that of simulation A only in that (1) $s_v = h_l$ in the buoyancy term of the resolvable-scale w equation, and (2) the subgrid flux of s_v equals that of h_l in the subgrid-scale kinetic energy equation, both *inside* and *outside* the cloud elements. Here s_v is the virtual dry static energy, h_l is the liquid water static energy as defined in Moeng (1986), and w is vertical velocity fluctuations. Throughout this paper, we will present these static energies in kelvins since they are divided by c_p, where c_p is the specific heat of air. (In the dry cloud simulations, we treat the liquid water static energy and the virtual dry static energy the same, even though the dry-cloud "liquid water" content q_l is not zero.) Thus, the differences between simulations A and B are due only to the latent heating, which is also discussed in section 3. The concept of a dust cloud has been used also by Lilly (1968). Simulation C excludes, in addition to latent heating, surface heating and longwave heating near the cloud base, thus, representing a prototype "dry" STBL that is driven primarily by cloud-top radiative cooling. This simulation, compared with a CBL simulation (Moeng and Wyngaard 1988), allows us to study the differences between the convective plumes that are driven by cloud-top radiative cooling and those driven by surface heating and is discussed in section 4. For reasons given in section 4, we perform simulation D, which is similar to simulation C, except that D has a negative buoyancy flux at the surface to mimic, in the upside-down sense, the negative entrainment flux at the top of the CBL case. Section 5 contains our summary and conclusions.

2. The 3D conditional sampling

We identify n eddies that have the strongest updrafts in terms of vertical velocity in a selected reference plane $z = z_{\text{ref}}$. Figure 1 shows an example of the x–y cross section at $z_{\text{ref}} = z_i/2$ of the simulated vertical velocity field. The composite updraft is formed by the following averaging:

$$f_u(x, y, z) = \frac{1}{m}\sum_{j=1}^{m}\frac{1}{n}\sum_{i=1}^{n} f(x_i + x, y_i + y, z, t_j), \quad (1)$$

where (x_i, y_i) are the locations (as marked in Fig. 1) of the n strongest updrafts at z_{ref} level, where $n = 36$ is the number of selected eddies, $m = 6$ is the number

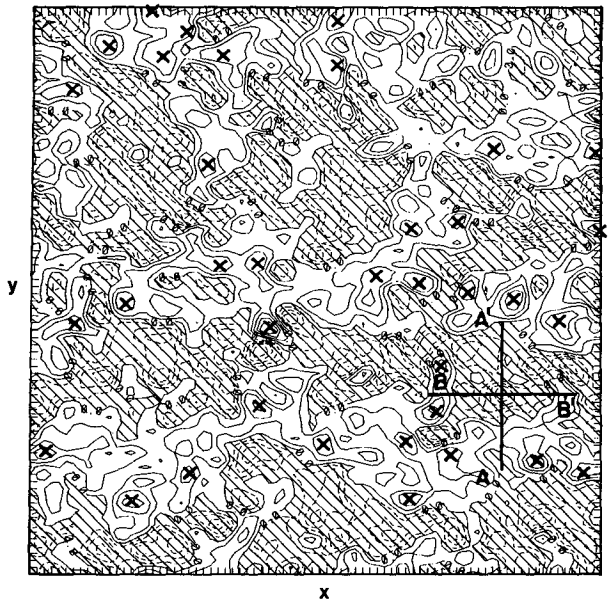

FIG. 1. An x–y cross section of the vertical velocity field at the mid-STBL. The strong updrafts that are selected for composite are marked by ×. The vertical cross sections between A and A′ and between B and B′ are shown in Fig. 2.

of recorded datasets for time averaging, and f_u is any field associated with the composite updraft. Note that z in (1) is a variable, while z_{ref} is fixed for each set of conditional sampling. Here z_{ref} should be chosen to be well within the turbulent layer for a composite structure that represents the main plumes within the mixed layer. A similar procedure is applied to form the composite downdraft. Readers are referred to Schmidt and Schumann (1989) for a more detailed description of the sampling technique.

Figure 2 shows a y–z cross section of the vertical velocity field and an x–z cross section near the center of the strongest downdraft. In all simulations, there is a 10 m s^{-1} geostrophic wind in the x direction; thus, there exists some vertical shear of the mean wind (mean profiles are shown in Schumann and Moeng 1991a). However, even with such mean shear, the eddies do not tilt much in the downwind direction (Fig. 2b). Most of the energetic eddies extend vertically from the surface to the top of the PBL. This instantaneous flow field is characterized by chaotic motion with considerable variability in the eddy structures. However, as we will see later, the composite field has a simple-looking shape that allows us to study *qualitatively* the eddy structure in an otherwise complex turbulence system. Through a different sampling technique, Schumann and Moeng (1991a, b) examine *quantitatively* the turbulent fluxes and budgets of all updrafts and downdrafts of simulation A.

In the rest of this text, "updraft" and "downdraft" refer to the composited structures, and the mean and transport fields shown are associated with the composite updraft and downdraft. Even though the details of the composite structure depend on the choice of z_{ref}, we will describe only the general characteristics that are independent of the choice of z_{ref}. Our choice of $z_{\text{ref}} = z_i/2$ seems to give the best representation of the most energetic updrafts and downdrafts.

3. The updraft and downdraft in simulations A and B

The overall characteristics of simulation A are reported in Schumann and Moeng (1991a): the averaged cloud-top height z_i is about 507 m; the vertical velocity scale $w_{c*} \equiv [(g/T_0)B_* z_i]^{1/3} \sim 0.8$ m s^{-1}; the temperature scale $T_* \equiv B_*/w_{c*} \sim 0.04$ K; and the moisture scale $Q_* \equiv M_*/w_{c*} \sim 0.02$ g kg^{-1}, where $B_* \equiv c_p^{-1} \int_{z_B}^{z_i} \overline{ws_v} dz/(z_i - z_B)$ and $M_* \equiv \int_{z_B}^{z_i} \overline{w(q_v + q_l)} \times dz/(z_i - z_B)$ are the vertically averaged buoyancy and moisture fluxes within the cloud layer; z_B is the cloud-base height (~200 m); and q_v and q_l are the concentrations of water vapor and liquid. The mean cloud-top height evolves from 504 to 510 m during

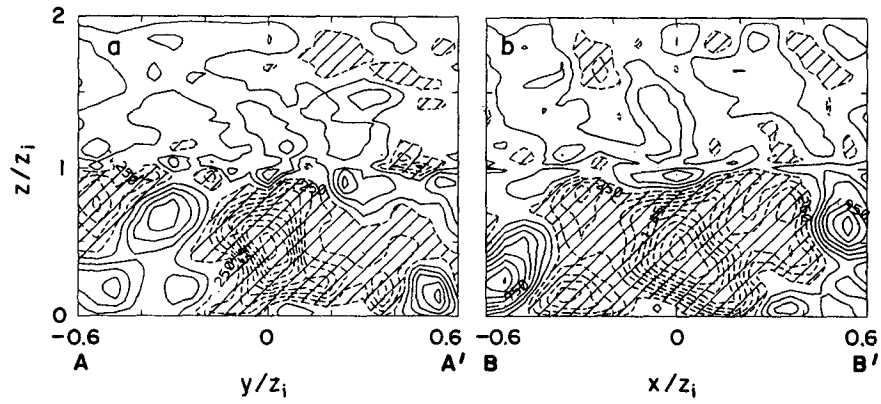

FIG. 2. The vertical cross sections of the vertical velocity field between (a) A and A′ and (b) B and B′, indicated in Fig. 1.

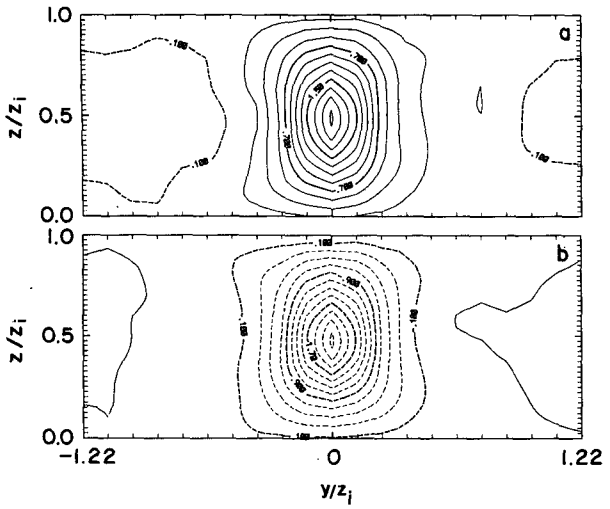

FIG. 3. The composite vertical velocity field of the (a) updraft and (b) downdraft of simulation A. The contour interval is 0.2.

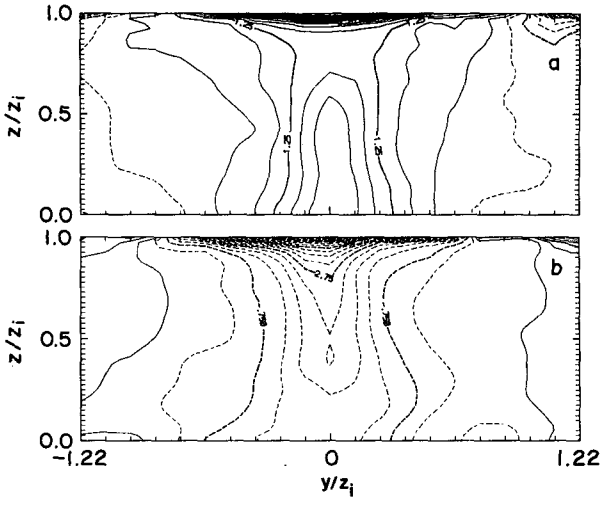

FIG. 5. Same as Fig. 3, but for the moisture fluctuations. The contour interval is 0.5. [The maximum contour in (a) is ~11.5 and the minimum in (b) is ~ −9.]

the last 1500-s simulation time and the large-scale subsidence at this height is about 0.15 cm s^{-1}; thus, the entrainment velocity is ~0.55 cm s^{-1}. The liquid water static energy (divided by c_p) increases from 286 to about 296 K across the cloud top, whereas the total water decreases from 7.2 to 4 g kg^{-1}. This corresponds to a jump of the equivalent potential temperature of about +2.2 K and a jump of the total water of −3.2 g kg^{-1}; therefore, this simulated cloud layer is stable with respect to the cloud-top entrainment instability (Lilly 1968; Deardorff 1980; Randall 1980; MacVean and Mason 1990).

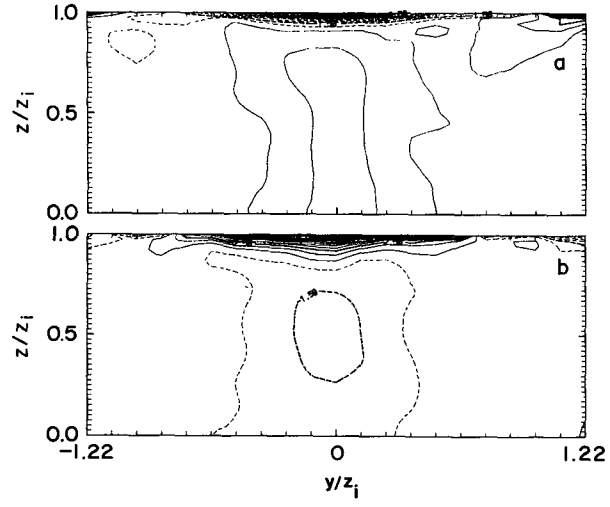

FIG. 4. Same as Fig. 3, but for the liquid water static energy fluctuations. The contour interval is 1. [The minimum contour in (a) is ~ −20.5 and the maximum in (b) is ~16.]

Figure 3 shows the vertical velocity field of the updraft and downdraft, normalized by w_{c*}. Here we choose to show the y–z cross section instead of x–z to exclude any possible complication due to the mean shear. The domain shown covers ~2.5 z_i in y and z_i in z; the horizontal extent covers the influence region of plumes, while the vertical extent is limited at $z = z_i$ for the purpose of comparing the upside-down symmetry of the updraft and the downdraft about the mid-PBL. Figure 3 shows that the updraft and downdraft have about the same vertical velocities; this is expected because this case has both cloud-top radiative cooling and surface heating. This feature differs from that of the CBL shown in Schmidt and Schumann (1989, their Fig. 18); in the CBL the updraft at z_{ref} is twice as strong as the downdraft there. Figure 3 implies that the vertical velocity skewness, $S_w \equiv \overline{w^3}/\overline{w^2}^{3/2}$, in the mid-PBL is about zero in simulation A, as opposed to a positive in the CBL.

Figures 4 and 5 show h_l/c_p and total moisture $q_v + q_l$ deviations from their total horizontal mean values. The thermal field is normalized by T_*, the moisture field by Q_*. (The s_v field is similar to the h_l field except that s_v has a sharper gradient at the tops of both updraft and downdraft.) The top ~10% of the updraft is much colder and moister, showing the penetration of the impinging updrafts into the inversion layer and the radiative cooling effect. There, the downdraft is much warmer and drier than its surroundings, showing that the inversion air is drawn into downdrafts.[1] These features show the entrainment process. Below this en-

[1] The mean cloud-top height averaged over the updraft is about 513 m and that over the downdraft is about 503 m. Hence, the top ~1% of the downdraft shown here is beyond the cloud top.

trainment zone, the updraft is $\sim 2T_*$ warmer and $\sim 2.5Q_*$ moister than its surroundings. The downdraft is $\sim -2T_*$ cooler than its surroundings since it carries the radiatively cooled (not evaporatively cooled, as discussed later when simulations A and B are compared) air downward; this is consistent with Nicholls' (1989) observational study that shows that the temperature deficiency within the downdrafts is about $-2T_*$ and is "almost entirely due to the incorporation of radiatively cooled air." Drier air within the downdraft extends from the entrainment zone all the way to the surface since radiation does not change the total moisture field.

Figure 6 shows the pressure fluctuations normalized by ρw_{c*}^2. Positive maxima exist in the upper part of the updraft and in the lower part of the downdraft, which is expected from the buoyancy and flow field distribution. Some positive fluctuations exist in the upper part of the STBL downdraft, which is surprising; contrarily, the pressure fluctuations are negative in the lower part of the CBL updraft "presumably caused by buoyant bubbles which suck in air from below and from sides" (Schmidt and Schumann 1989). We will discuss this difference more in section 4.

Figures 7 and 8 show the vertical transports of liquid water static energy and moisture (normalized by $c_p B_*$ and M_*, respectively); they are computed by correlating the h_l/c_p and $q_v + q_l$ fields with w and include the corresponding subgrid-scale (SGS) fluxes. (The SGS components are negligibly small, even when $z_{ref} \sim 0.1\ z_i$ is chosen.) Figures 7 and 8 indicate that the updraft and downdraft contribute equally to the turbulent transport. Figure 7 also shows that about $-3B_*$ downward heat flux resides in the upper updraft, while only about $-B_*$ resides in the upper downdraft; in other words, the entrainment flux results more from the penetration of updrafts into the inversion layer, less due to the downdrafts pulling warm air down.

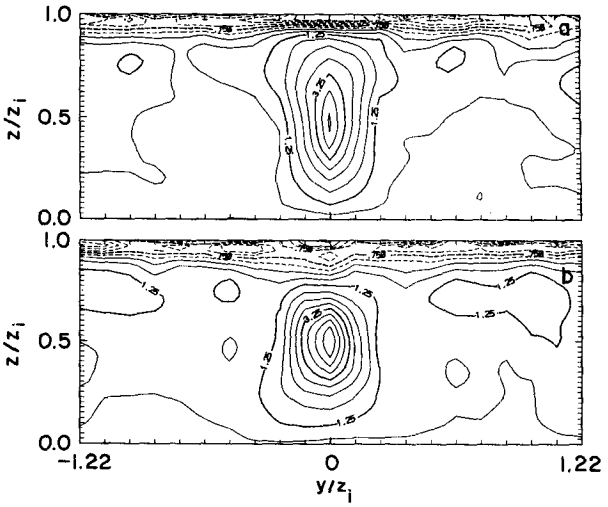

FIG. 7. Same as Fig. 3, but for the transport of the liquid water static energy. The contour interval is 0.5.

The structure discussed so far is consistent with most observations of the convective plumes in the CBL (e.g., Stull 1988) and in the STBL (e.g., Caughey and Kitchen 1984; Nicholls 1989), except that we do not see a region near cloud top where the plumes form a cellular pattern with narrow downdrafts surrounded by broad updrafts as observed by Nicholls. This discrepancy may be due to the limited resolution of LES. Another discrepancy is that Caughey and Kitchen observed a clearly positive correlation between vertical velocity and temperature fluctuations very close to the cloud top ($z \sim 0.99 z_i$), while we show that only after

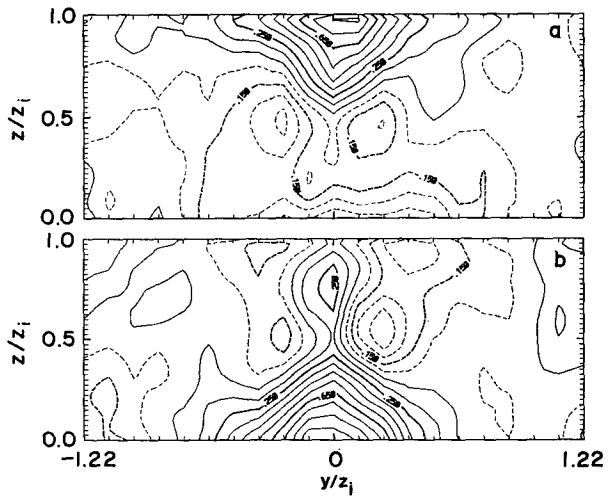

FIG. 6. Same as Fig. 3, but for the pressure fluctuations. The contour interval is 0.1.

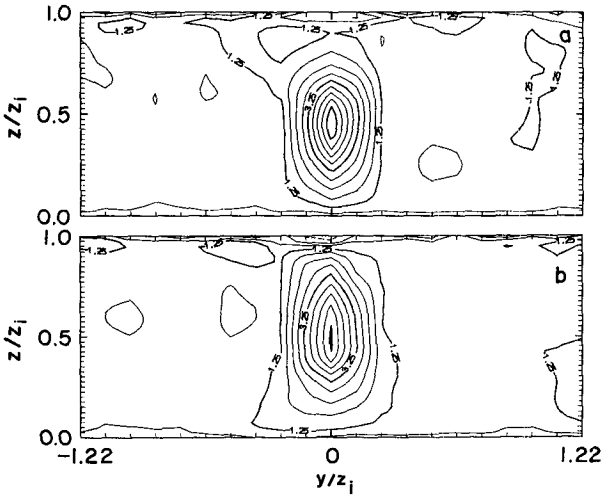

FIG. 8. Same as Fig. 3, but for the moisture transport. The contour interval is 0.5.

some distance away from the cloud top ($z \sim 0.9z_i$), does the correlation become clearly positive. This difference cannot be explained simply by the horizontal variations of the cloud-top height, since the simulated cloud-top heights do not vary more than $0.05z_i$. Our simulation shows that at a height close to the cloud top but *within* the cloud, vertical velocity and temperature fluctuations are slightly negatively correlated. This discrepancy may be due to the fact that the LES results include only the larger-eddy contributions to the turbulent fluxes and entrainment process, while the tethered balloon results, which consist of 5-min averages, include only smaller eddies.

Next, we analyze other simulations that are designed to isolate the physical processes involved. They represent a hypothetical, idealized STBL and allow investigation of features that are difficult to access through measurements.

Simulation B is designed to study just the latent-heating effect. It is similar to simulation A, except that the cloud does not undergo phase change; in effect it is like a dust cloud that affects the turbulent motion only through radiative exchange. We compare the composite structures and observe no significant difference between these two simulations in the sense that all of the qualitative features described above still hold for simulation B. (There are a few quantitative differences, e.g., the downdraft is now $\sim -3T_*$ cooler than its surroundings, the negative heat flux at the updraft top is only about $-1.5B_*$, and the downdraft top is about $-0.4B_*$.) It appears that, at least in this "stable" case, in the context of cloud-top entrainment instability, latent heating is less important for determining the structure than surface heating and cloud-top radiative cooling.

4. Cloud-top–cooled STBL versus surface-heated CBL

In simulation C, we reduce the surface temperature such that the surface buoyancy flux is nearly zero. In addition, the radiative heating/cooling rate is set to zero below the fifth grid down from the local cloud top at each grid column; this excludes the cloud-base warming. However, the exclusion of this warming (which is small anyway; see Schumann and Moeng 1991a) does not seem to make any significant difference in composite structure. We exclude the latent heating also. Simulation C therefore represents a prototype PBL that is driven solely by the cloud-top cooling. (Note that the shear is weak.)

We also analyze the composite structure of a CBL simulation by Moeng and Wyngaard (1988), where the CBL turbulence is driven by an imposed surface buoyancy flux of 240 W m^{-2}. This simulation was generated from Moeng's LES code that has different numerics from the LES code used by Schmidt and Schumann (1989), but both result in very similar

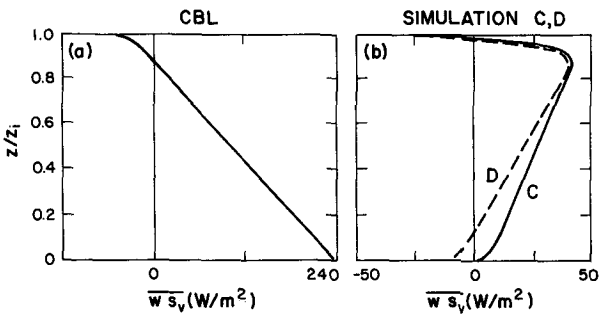

FIG. 9. The vertical distributions of the total buoyancy flux for (a) the CBL simulation and (b) simulations C and D.

composite structures. Also, the CBL in Schmidt and Schumann is shear free; thus, this similarity indicates the minor importance of shear for this case. For consistency, however, simulation C is directly compared to the CBL generated by Moeng and Wyngaard. The CBL turbulence is driven solely by the surface heating.

Figure 9 compares the total buoyancy flux profiles of (a) the CBL and (b) the simulation C cases; the former has a maximum at the surface and decreases upward, while the latter has a maximum near the cloud top and decreases downward.

The composite structures of the CBL are shown in the left panels of Figs. 10–14, and those of simulation C are in the right panels. The normalization factors for the CBL are the convective velocity and temperature scales, given in Moeng and Wyngaard (1988). In all these figures, we compare the top left panel (the updraft in the surface-heated case) with the bottom right panel (the downdraft in the cloud-top–cooled case), and, similarly, the bottom left is compared with the top right. The asymmetry between the cloud-top–cooled and the surface-heated cases should be mainly due to the asymmetry of the entraining-interface top and the rigid bottom (with friction) and may be partly due to the different vertical distributions of the cloud-top–cooling and the surface heating.

The vertical velocity field shown in Fig. 10b is surprising: in simulation C where there is no surface heating, the cooling-generated downdraft is only slightly stronger than its compensating updraft (i.e., about $-2.4w_{c*}$ vs $+2.2w_{c*}$).[2] This is very different from the surface-heating–only case, where the heating-generated updraft is almost twice as strong as the compensating downdraft (i.e., about $+1.8w_*$ vs $-1.1w_*$; Fig. 10a).

[2] This finding is consistent with the distribution of the vertical velocity skewness from a large-eddy simulation of a STBL with no surface flux (Moeng 1986): instead of being negative everywhere as intuitively expected, the vertical velocity skewness is positive in the upper one-third and negative in the lower two-thirds of the layer, being only slightly negative in the mid-PBL.

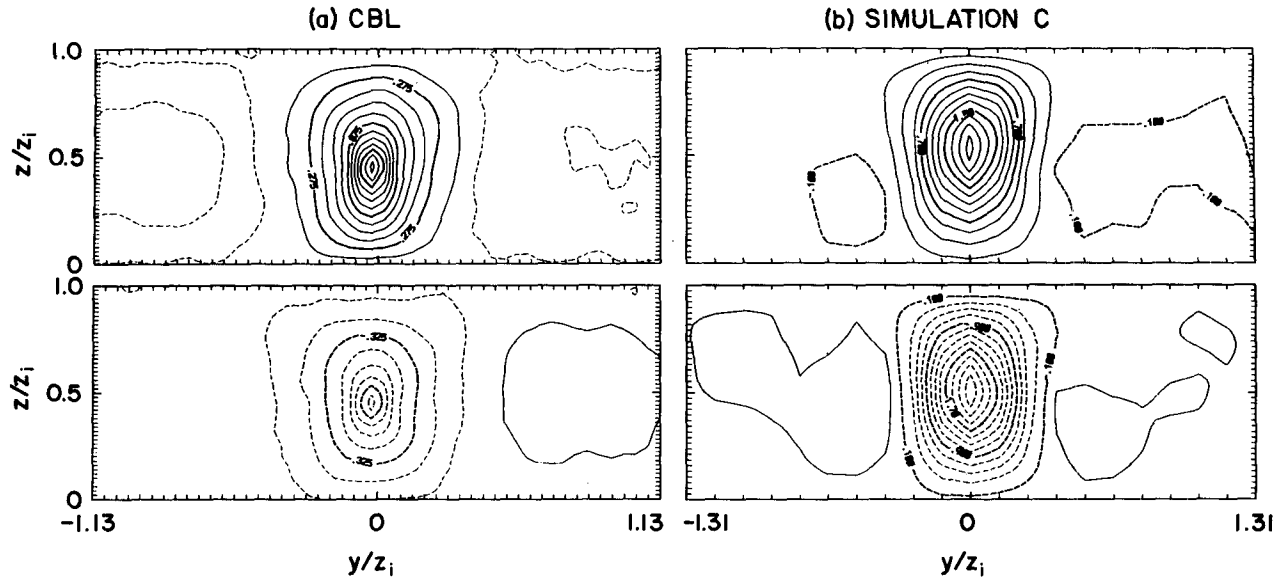

FIG. 10. The vertical velocity field of the updraft (upper panels) and the downdraft (lower panels) for (a) the CBL simulation and (b) simulation C. The contour interval is 0.15 for the CBL and 0.2 for simulation C.

Figure 11, the virtual dry static energy (divided by c_p) shows more asymmetry in the composite structures between the surface-heated and cloud-top–cooled cases. The most significant difference lies in the vertical distribution of the temperature fluctuations. For the cloud-top–cooled case, the temperature fluctuations are well correlated with the vertical velocity fluctuations within both updraft and downdraft; for the surface-heated case, the temperature fluctuations are well correlated with the vertical velocity only within the updraft. In the CBL, the minimum temperature fluctuations of the downdraft are near the surface.

This leads to a significant difference in the vertical heat transport, as shown in Fig. 12. In the surface-heated case, the downdraft contributes almost nothing, while in the cloud-top–cooled case, the updraft contributes significantly. This does not imply that all of the heat transfer is due to the updrafts in the surface-

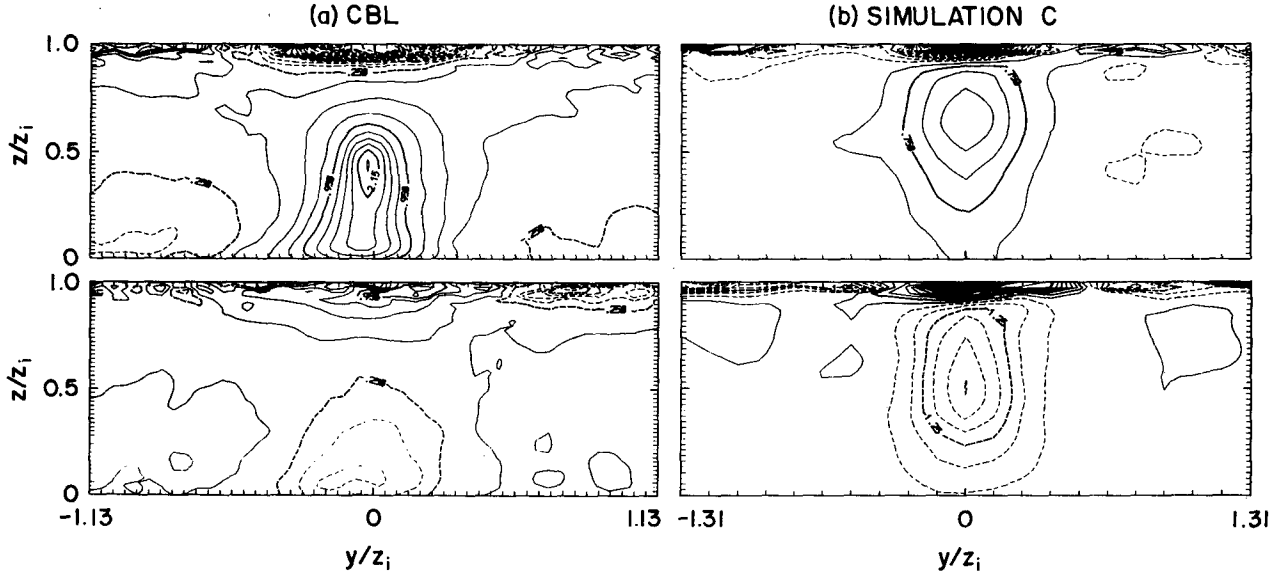

FIG. 11. Same as Fig. 10, but for the fluctuations of the virtual dry static energy. The contour interval is 0.3 for the CBL and 0.5 for simulation C. (The minimum contour is ~ −4 in the upper left figure and ~ −12 in the upper right. The maximum contour is ~5 in the lower right.)

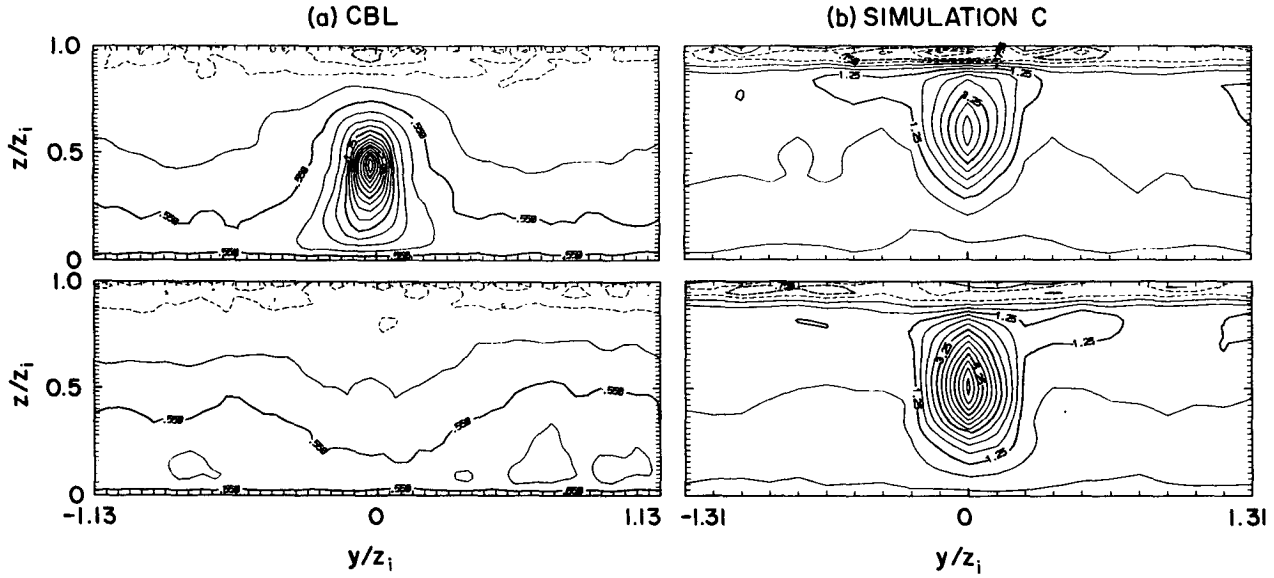

FIG. 12. Same as Fig. 10, but for the buoyancy transport. The contour interval is 0.3 for the CBL and 0.5 for simulation C. (In simulation C, the negative flux at the updraft top is about $-2.3B_*$, while that at the downdraft top is about $-0.3B_*$.)

heated case because we consider only a subset of strong updrafts and downdrafts. Observations (e.g., Greenhut and Khalsa 1987) and our LES results (from the velocity–temperature joint probability density and from the sampling analysis in Schumann and Moeng 1991a) show that in the CBL, *total* updrafts contribute about 70% of the heat transport and *total* downdrafts contribute about 30%. As implied by Fig. 12, this 30% contribution from the downdrafts comes mainly from weak downdrafts, not the strong downdrafts that are selected for our composites.

This is also true for the momentum transports (Fig. 13). All our simulations have a 10 m s^{-1} geostrophic wind in the x direction, thus, the net u-momentum transport is downward. In the surface-heated case, the downdraft contributes nothing to the downward transport, but in the cloud-top–cooled case, the updraft contributes significantly.

Figure 14 compares the pressure fluctuations (normalized by ρw_*^2 and ρw_{c*}^2, respectively, for the CBL and simulation C). In the lower part of the CBL updraft, the pressure fluctuations are negative, but in the

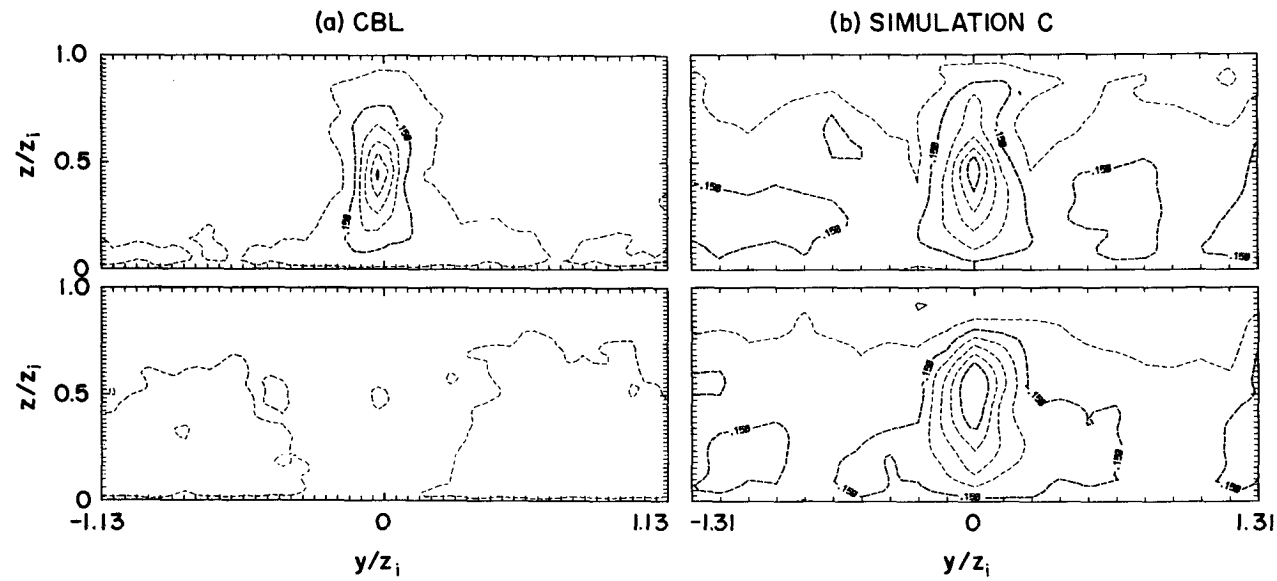

FIG. 13. Same as Fig. 10, but for the momentum transport. The contour interval is 0.1 for both cases.

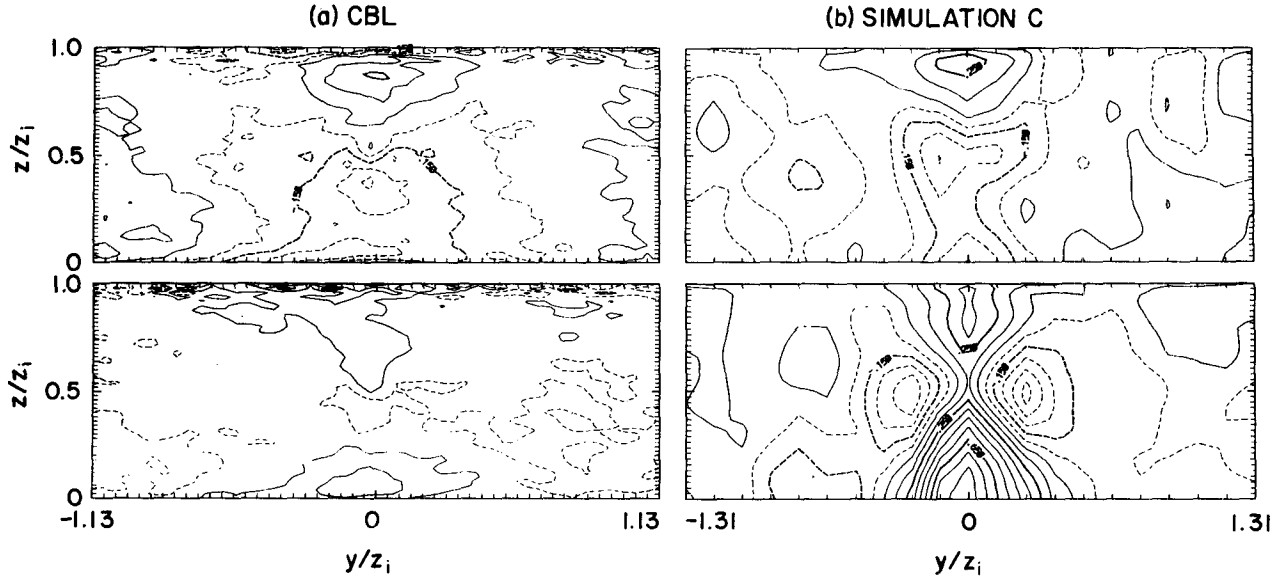

FIG. 14. Same as Fig. 10, but for the pressure fluctuations. The contour interval is 0.1 for both cases.

upper part of the cloud-top-cooled downdraft, they are positive. This asymmetry implies that the CBL updrafts are buoyantly accelerated, thus sucking air up, but the STBL downdrafts are dynamically forced as the horizontal motion converges near the interface; this is also suggested by Nicholls' (1989) observations.

A difference between the CBL simulation and simulation C is that the former has a negative buoyancy flux at the top, while the latter has zero flux at the bottom (Fig. 9). We first asked whether this difference results in the asymmetry between the two cases; this led us to perform another simulation, D, with an imposed negative buoyancy flux at the surface. We used a surface flux of -10 W m^{-2} that is about -0.2 of the maximum flux near the cloud top, which is the ratio of the entrainment/surface fluxes in the CBL case; this buoyancy flux profile is also shown in Fig. 9. In simulation D, the heat and moisture transports in the updraft become smaller comparing with simulation C (not shown), but the updraft is still nearly as strong as the downdraft and the updraft still contributes somewhat to the vertical transport.

We therefore look into other mechanisms. We examine the flow fields of individual plumes near the cloud top in simulation D. Figure 15 shows a y–z cross section of the liquid water, virtual dry static energy fluctuations (divided by c_p), and vertical velocity fields between $0.85 < z/z_i < 1.05$. The v–w velocity vectors are also plotted in Fig. 15b. The temperature minima and liquid water content maxima are strongly correlated (they agree with observations, e.g., Nicholls and Turton 1986) and are found mostly at the top of penetrating updrafts. When updrafts (formed as a return flow of downdrafts) impinge onto the inversion layer, the upward vertical motion converts to horizontal motion, and the horizontal motion converges and generates downdrafts in between two neighboring penetrating updrafts (e.g., the updrafts at $y \sim 3$ km and 4 km and the downdraft at $y \sim 3.4$ km). Downdrafts that form this way—as opposed to forming as the most radiatively cooled air sinks—carry *both* radiatively cooled air and entrained warm air. This is supported by Nicholls (1989), who observed large temperature fluctuations inside the near cloud-top downdrafts. Warm air within the downdrafts cannot travel far into the STBL (because it is buoyantly decelerated), while cold air within can, before both air types become completely mixed. Most of the downdrafts, after reaching a certain distance from the cloud top ($\sim 0.9z_i$ or even farther down), become cooler than the environment and become buoyancy driven.

To demonstrate this more clearly, we drew a sketch in Fig. 16 that summarizes this physical picture. Three points are emphasized: 1) the coldest air near the cloud top exists on top of updrafts, due to the adiabatic lifting and the least amount of entraining air there, and could also be due to a larger radiative-cooling rate since the liquid water content is larger there. 2) The STBL downdrafts are driven, *at their root,* dynamically by the convergence of the horizontal flow, rather than buoyantly. 3) Radiative cooling and entrainment processes interact before the cooling starts to drive the turbulence circulation. In other words, the entrainment process modifies the efficiency of the energy production due to cloud-top cooling.

These are contrary to the CBL: 1) the warmest air near the surface tends to gather near the root of the CBL updrafts, 2) the updrafts are driven mainly by the buoyancy at their root and throughout most of the CBL, and 3) the surface heating drives the turbulence

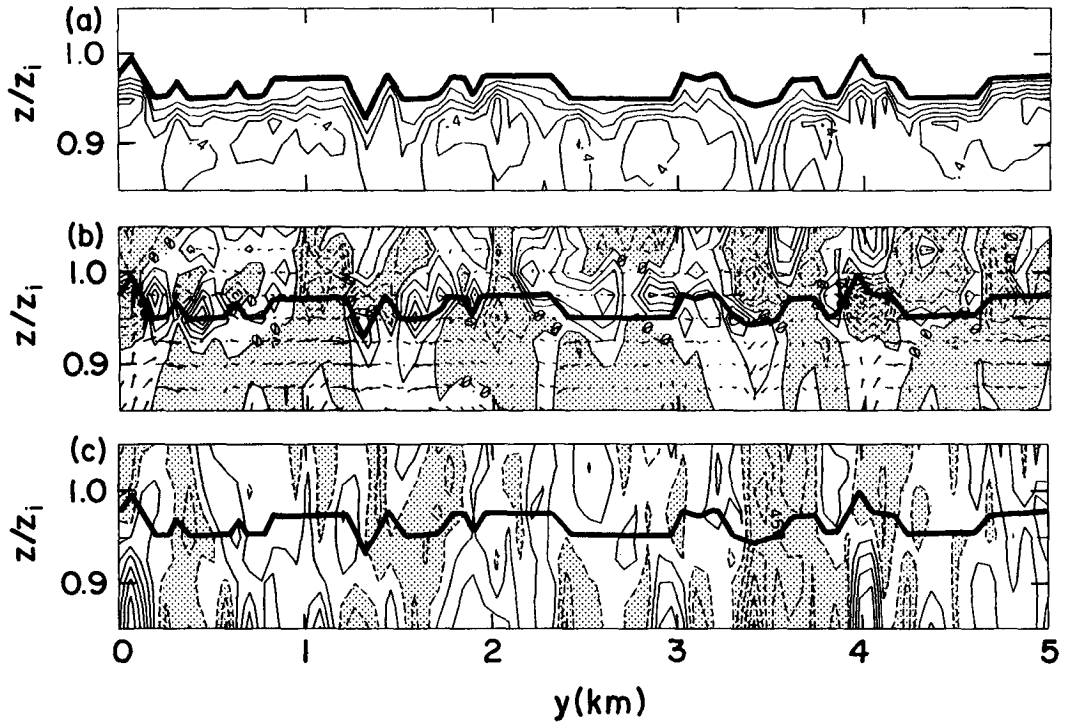

FIG. 15. A y–z cross section of (a) the liquid water mixing ratio, (b) the virtual temperature fluctuations and the v–w vector plot, and (c) the vertical velocity in simulation D. The negative areas are shaded. The solid curve represents the cloud top in all panels.

circulation, and, consequently, the circulation promotes the entrainment process.

This physical picture explains the asymmetry of the composite features between the cloud-top–cooled and surface-heated cases that we have found. If the STBL downdraft at its root is driven mainly by the convergence of horizontal motion, which results from the conversion of updraft motion, the downdraft is unlikely to become much stronger than the updraft. In contrast, the CBL updraft near its root is driven mainly by the buoyancy; thus, it can become much stronger than the compensating downdraft (Fig. 10). The STBL downdraft at its root is warmer than its surroundings and becomes colder (due to the remaining radiatively cooled air) only below the entrainment zone ($\sim 0.9 z_i$). The CBL updraft is always warmer than the surroundings, at its root and throughout most of the CBL (Fig. 11). The STBL pressure fluctuations are positive in the upper part of the downdraft due to the horizontal flow convergence; the CBL pressure fluctuations are negative in the lower part of the updraft due to the buoyancy acceleration (Fig. 14).

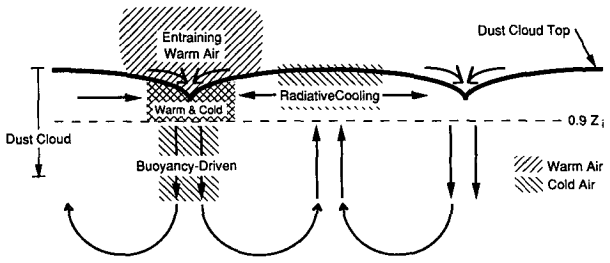

FIG. 16. A sketch of our physical picture showing the idealized flow field (in arrows) and temperature fluctuations near the STBL top. Different shading signifies different temperature fluctuations. This sketch emphasizes only the locations where the longwave radiative cooling is strongest and where the warm air entrainment is largest.

The turbulence-kinetic-energy budgets from observations (Nicholls 1989) and LES (Moeng 1986) both show that in the near cloud-top layer the pressure transport term is the major source of energy consistent with our physical picture. In their conditional-sampling budget analysis for the STBL, Schumann and Moeng (1991b) also show that downdrafts near the inversion gain most of their kinetic energy from updrafts through the lateral exchange across the updraft–downdraft interface.

5. Summary and conclusions

A 3D conditional sampling technique is applied to four large-eddy simulated turbulent flows of STBL to examine the structure of plumes within the STBL. This sampling technique identifies the spatial fields of main updrafts and downdrafts. In simulation A, which in-

cludes surface heating, radiative cooling, and latent heating, the composite downdraft is as strong as the composite updraft, and both contribute about the same to the turbulent transports of heat, moisture, and momentum. This is expected since there is about an equal amount of surface heating and cloud-top cooling. The mean thermal and moisture fields within the updraft and the downdraft reflect features of the entraining process and the dominant effect of radiative cooling on the downdraft. Simulation B is similar to A except that the latent-heating effect is excluded; by comparing simulations A and B, we conclude that in the cases that are stable with respect to the cloud-top entrainment instability, the latent-heating effect has little influence on the plume structure.

In simulations C and D, which are driven entirely by the cloud-top radiative cooling, the updraft (which is supposed to be the compensating motion) has about the same strength as the downdraft (which is supposed to be the primary plume) and also contributes a significant amount of the heat, moisture, and momentum fluxes. This is surprising since there is only cloud-top cooling and no surface heating. For comparison, the composite structure of a CBL that is driven by the surface heating only is shown; in this case, the downdraft (i.e., compensating motion) is much weaker than the updraft (i.e., primary plume) and contributes very little to the heat, moisture, and momentum fluxes. This asymmetric feature between the cloud-top–cooled and surface-heated cases may result from the following mechanism: the STBL downdrafts near the cloud top carry both radiatively cooled air and entrained warm air and are not *initially* forced as cold air sinks. Rather, these downdrafts are initially forced as the horizontal motion converges. The forcing is affected by the vertical pressure gradients that result from the horizontal convergence. Only after these downdrafts move a certain distance down from the entrainment zone, most of them become colder than the environment due to the remaining radiatively cooled air and thus become buoyantly driven. In contrast, the CBL updrafts are forced mainly by buoyancy force at their roots and throughout most of the turbulent layer; these updrafts carry only warmer-than-environment air until they reach the inversion layer.

This asymmetric property is likely to play an important role in the entrainment process. It is generally accepted that in the CBL the entrainment process is greatly enhanced by the strong updrafts that penetrate the interface. Laboratory experiments (e.g., Deardorff et al. 1969) and observations (e.g., Kaimal et al. 1976) indicate that the entrainment process occurs as the domes of the overshooting updrafts spread out and "wisps" of fluid from above are folded into the turbulent layer. In other words, the penetrating updrafts are actively responsible for the entrainment, and downdrafts only passively drag the entrained air into the turbulent layer. Figure 12a shows that most of the negative entrainment heat flux resides in the uppermost part of the updraft. In the cloud-top–cooled case, the updraft also actively drives the entrainment process, and the negative entrainment heat flux near the STBL top also resides more in the uppermost part of the updraft (Fig. 12b), even though the updraft is not the primary plume. The entrainment process can be as vigorous in the cloud-top–cooled case because in this case the updraft is as vigorous as the downward plumes directly generated by cooling, as found in this study.

The asymmetry also suggests that many of the CBL modeling concepts are not applicable to the STBL, such as the entrainment hypotheses used in the mixed-layer modeling, discussed in Moeng (1987). In the CBL, the surface heating drives the turbulent circulations, and the updrafts of these circulations promote the entrainment process. Thus, the entrainment process is only a consequence of the surface heating, and the entrainment buoyancy flux is almost always about −20% of the surface buoyancy flux. However, the mechanism is different in the STBL. It consists of the following three steps: 1) the entrainment process modifies the radiatively cooled air parcels near the cloud top, 2) these modified air parcels form downdrafts that drive the turbulent circulations, and finally 3) the updrafts resulting from these circulations promote the entrainment process. A larger entrainment rate may therefore reduce the efficiency of turbulence–kinetic-energy production due to radiative cooling, which in turn may slow the entrainment rate. This feedback mechanism is complicated, and, therefore, developing a scheme (i.e., a hypothesis) for the entrainment process in the STBL remains a difficult problem. One approach might be developing a dynamical model based on the budget equations for updrafts and downdrafts as studied in Schumann and Moeng (1991b).

The simulated stratus cloud layers we have analyzed are all stable with respect to the cloud-top entrainment instability. When the cloud layer is subject to such an instability, both thermal and moisture fields of the downdraft are expected to be different from those shown in this paper, since the evaporative cooling process dominates. This type of analysis, therefore, could be useful for detecting the instability processes. We plan to study it in the future.

In the case of decoupling between the stratus and its subcloud layers (e.g., Turton and Nicholls 1987) the composite structure may not extend throughout the whole boundary layer. To study the decoupling case, we need to include solar radiation into the LES code.

Acknowledgments. We thank Alan Betts, Chris Bretherton, Chris Fairall, Siri Khalsa, Don Lenschow, Dave Randall, Rich Rotunno, and George Young for their helpful comments. This work was partially supported by the Office of Naval Research under Interagency Agreement (IA) No. 89-12.

REFERENCES

Caughey, S. J., and M. Kitchen, 1984: Simultaneous measurements of the turbulent and microphysical structure of nocturnal stratocumulus cloud. *Quart. J. Roy. Meteor. Soc.*, **110,** 13–34.

Deardorff, J. W., 1980: Cloud top entrainment instability. *J. Atmos. Sci.*, **37,** 131–147.

——, G. E. Willis and D. K. Lilly, 1969: Laboratory investigation of nonsteady penetrative convection. *J. Fluid Mech.*, **35-1,** 7–31.

Greenhut, G. K., and S. J. S. Khalsa, 1987: Convective elements in the marine atmospheric boundary layer. Part I: Conditional sampling statistics. *J. Climate Appl. Meteor.*, **26,** 813–822.

Kaimal, J. C., J. C. Wyngaard, D. A. Haugen, O. R. Coté, Y. Izumi, S. J. Caughey and C. J. Readings, 1976: Turbulence structure in the convective boundary layer. *J. Atmos. Sci.*, **33,** 2152–2169.

Lenschow, D. H., and P. L. Stephens, 1980: The role of thermals in the convective boundary layer. *Bound.-Layer Meteor.*, **19,** 509–532.

Lilly, D. K., 1968: Models of cloud-topped mixed layers under a strong inversion. *Quart. J. Roy. Meteor. Soc.*, **94,** 292–309.

MacVean, M. K., and P. J. Mason, 1990: Cloud top entrainment instability through small-scale mixing and its parameterization in numerical models. *J. Atmos. Sci.*, **47,** 1012–1030.

Mahrt, L., 1979: Penetrative convection at the top of a growing boundary layer. *Quart. J. Roy. Meteor. Soc.*, **105,** 469–485.

Moeng, C.-H., 1984: A large-eddy-simulation model for the study of planetary boundary-layer turbulence. *J. Atmos. Sci.*, **41,** 2052–2062.

——, 1986: Large-eddy simulation of a stratus-topped boundary layer. Part I: Structure and budgets. *J. Atmos. Sci.*, **43,** 2886–2900.

——, 1987: Large-eddy simulation of a stratus-topped boundary layer. Part II: Implications for mixed-layer modeling. *J. Atmos. Sci.*, **44,** 1605–1614.

——, and A. Arakawa, 1980: A numerical study of a marine subtropical stratus cloud layer and its stability. *J. Atmos. Sci.*, **37,** 2661–2675.

——, and J. C. Wyngaard, 1988: Spectral analysis of large-eddy simulations of the convective boundary layer. *J. Atmos. Sci.*, **45,** 3573–3587.

Nicholls, S., 1989: The structure of radiatively driven convection in stratocumulus. *Quart. J. Roy. Meteor. Soc.*, **115,** 487–511.

——, and J. D. Turton, 1986: An observational study of the structure of stratiform cloud sheets: Part II. Entrainment. *Quart. J. Roy. Meteor. Soc.*, **112,** 461–480.

Randall, D. A., 1980: Conditional instability of the first kind upside-down. *J. Atmos. Sci.*, **37,** 125–130.

Rodgers, C. D., 1967: The use of emissivity in atmospheric radiation calculation. *Quart. J. Roy. Meteor. Soc.*, **93,** 43–54.

Schmidt, H., and U. Schumann, 1989: Coherent structure of the convective boundary layer derived from large-eddy simulations. *J. Fluid Mech.*, **200,** 511–562.

Schumann, U., and C.-H. Moeng, 1991a: Plume fluxes in clear and cloudy convective boundary layers. *J. Atmos. Sci.*, **48,** 1746–1757.

——, and ——, 1991b: Plume budgets in clear and cloudy convective boundary layers. *J. Atmos. Sci.*, **48,** 1758–1770.

Stull, R. B., 1973: Inversion rise model based on penetrative convection. *J. Atmos. Sci.*, **30,** 1092–1099.

——, 1988: *An Introduction to Boundary Layer Meteorology.* Kluwer Academic, 666 pp.

Turton, J. D., and S. Nicholls, 1987: A study of the diurnal variation of stratocumulus using a multiple mixed layer model. *Quart. J. Roy. Meteor. Soc.*, **113,** 969–1009.

Young, G. S., 1988: Turbulence structure of the convective boundary layer. Part II: Phoenix 78 Aircraft observations of thermals and their environment. *J. Atmos. Sci.*, **45,** 727–735.